Inducing Ferroquadrupolar Order with Applied Magnetic Field in $TbPO_4$

Paola Caterina Forino,[1,2,*] Jens Jensen,[3] Jian Rui Soh,[2,4,5] Sonia Francoual,[6] Oksana Zaharko,[7] Steffen Sloth,[1] Alexandra Turrini,[2,7] Ralf Feyerherm,[8] Karel Prokes,[8] Sofie Holm-Janas,[1] Ivica Zivkovic,[2] Yong Liu,[2] Arnaud Magrez,[2] Niels Bech Christensen,[1] Henrik M. Rønnow,[2,3] and Rasmus Toft-Petersen[1,9,†]

[1]*Department of Physics, Technical University of Denmark, 2800, Kongens Lyngby, Denmark*
[2]*Institute of Physics, École Polytechnique Fédérale de Lausanne (EPFL), 1015 Lausanne, Switzerland*
[3]*Niels Bohr Institute, Universitetsparken 5, DK-2100 Copenhagen, Denmark*
[4]*Quantum Innovation Centre (Q.InC), Agency for Science, Technology and Research (A*STAR), 2 Fusionopolis Way, Singapore 138634, Singapore*
[5]*Center for Quantum Technologies, National University of Singapore, 3 Science Drive 2, Singapore 117543, Singapore*
[6]*Deutsches Elektronen-Synchrotron (DESY), D-22607 Hamburg, Germany*
[7]*PSI Center for Neutron and Muon Sciences, Forschungsstrasse 111, 5232 Villigen, PSI, Switzerland*
[8]*Helmholtz-Zentrum Berlin für Materialien und Energie GmbH, 14109 Berlin, Germany*
[9]*European Spallation Source ERIC, P.O. Box 176, SE-221 00, Lund, Sweden*

(Received 27 August 2025; revised 5 December 2025; accepted 2 January 2026; published 6 February 2026)

In this work, we demonstrate a remarkable field-induced ferroquadrupolar phase emanating from the magnetoelastic coupling. Using synchrotron x-ray and neutron diffraction, heat capacity measurements, as well as mean-field modeling, we show that above the critical magnetic field, ferroquadrupolar O_2^{-2} order is stabilized as the main order parameter, in competition with the field-induced magnetic polarization. This is revealed by a severe lattice distortion and the suppression of antiferromagnetic ordering of the dipole moments. Even in zero magnetic field, the previously reported antiferromagnetic order is a mixed quadrupolar-dipolar phase, further highlighting the crucial role of spin-lattice interactions. This complete understanding of the magnetoelastic phase diagram establishes $TbPO_4$ as a model system for studying nematic-antiferromagnetic transitions and provides key Hamiltonian parameters for its description.

DOI: 10.1103/bhgt-jkj7 Subject Areas: Condensed Matter Physics, Magnetism

I. INTRODUCTION

The unquenched orbital electronic angular moment in magnetic f-electron systems occasionally gives rise to ordering of higher-order moments [1–4]. This is often referred to as *hidden order* due to the difficulty of detecting such a phase by conventional methods, which are usually sensitive to dipolar moments. Yet, hidden order can produce a plethora of exotic phenomena. Atomic multipoles in a crystal lattice can be strongly correlated and give rise to exotic phases such as quantum octupole liquids in the pyrochlore lattice of $Ce_2Sn_2O_7$ [5]. Quadrupolar fluctuations have even been suggested as a pairing mechanism for superconductivity, as in the case of $PrOs_4Sb_{12}$ [6] or $PrTi_2Al_{20}$ [7].

The higher-order magnetic moment is associated with a nonspherical distribution of unpaired f-shell electrons and as a result, the multipole order parameter is often coupled to the crystal lattice. This interplay between electronic, magnetic, and lattice degrees of freedom can give rise to nematic ferroquadrupolar (FQ) phase transition, driven by the local electronic interactions that break the rotational symmetry of the lattice, as in the case of intermetallic compounds such as $TmAg_2$ [8], and in the rare-earth zircons [9].

In the rare-earth zircons, the $RX\,O_4$ family, where R is a rare-earth element and X is V, As, or P, the quadrupole-quadrupole coupling is a phonon mediated indirect interaction and the quadrupolar order is accompanied by a uniform strain [10,11]. Here, the symmetry breaking of the strain reveals the symmetry of the coupled quadrupoles, as in the case of $DyVO_4$ [12] or $TmVO_4$ [9,13]. These compounds have been studied because of their magnetoelastic coupling and tunable quadrupolar interactions. Increasing interest in these systems has recently been driven by the realization that they can host quantum critical points, where the suppression of quadrupolar order leads to nontrivial electronic and structural fluctuations [9,14,15].

*Contact author: forino@fysik.dtu.dk
†Contact author: rasp@fysik.dtu.dk

$TbPO_4$ is a unique member of the rare-earth zirconium family, displaying a magnetoelectric coupling between the applied magnetic field and the electric polarization (and *vice versa*) that is among the strongest known in bulk magnetic materials, with a magnitude of 730 ps/m [16]. This strong coupling develops in the low-temperature antiferromagnetically ordered phase and is mediated by strain in the lattice [17]. As a consequence, a comprehensive understanding of the magnetoelastic Hamiltonian and the response of the lattice when an external field is applied is crucial to investigate the origin of the extraordinary magnetoelectric effect in $TbPO_4$ and the recently observed magnetoelectric fluctuations near the phase boundary [18]. The magnetic Hamiltonian of $TbPO_4$ [19] exhibits several magnetoelastic terms leading to unconventional magneto-structural phase diagrams and multiple low-energy crystal electric field (CEF) excitations at 0.4, 1.2, and 3.0 meV [20]. The importance of several excited CEF states, even at low temperatures, combined with a complex magnetoelastic Hamiltonian, makes $TbPO_4$ a modeling challenge.

$TbPO_4$ has a tetragonal zirconic structure with space group 141, $I4_1/amd$. Upon cooling, two transitions very close in temperature are encountered [21]. Below $T_N = 2.28$ K, $TbPO_4$ orders antiferromagnetically (AFM), with dipole moments along the crystallographic c axis, while at $T_S = 2.13$ K, a collinear tilt of the ordered moments is accompanied by a lattice distortion. When a magnetic field is applied along the easy axis c, at $B_1 \simeq 0.6$ T (for $T \simeq 1$ K) a phase transition—previously conjectured to be a spin-flop (SF) phase [22]—is identified. For fields $B_2 \simeq 1.1$ T, $TbPO_4$ becomes a polarized paramagnet.

Here, we study the phase diagram of $TbPO_4$ directly using synchrotron x-ray diffraction on single crystals. Neutron diffraction techniques, along with heat capacity and magnetization measurements, are also employed to explore the interplay between elastic and magnetic properties.

We investigate the lattice strains as evidence for quadrupole-quadrupole couplings in $TbPO_4$ in both zero and magnetic field applied along the c axis, hence determining the parameters of the magnetoelastic Hamiltonian. We present a new magnetoelastic phase diagram, shown in Fig. 1. In the zero-field antiferromagnetic phase below T_S, we detect two distinct strain components, which in turn reveal two distinct symmetries of quadrupolar ordering coexisting with the tilted antiferromagnetic (TAFM) dipole order. When the magnetic field is applied along the c axis, this striking complexity is replaced by a single FQ order parameter at a first-order phase transition, in competition with the field-induced magnetic polarization. This study highlights the crucial interplay between magnetic order and lattice distortions in $TbPO_4$, demonstrating how complementary techniques can indirectly reveal hidden order through strain-mediated interactions between quadrupole moments.

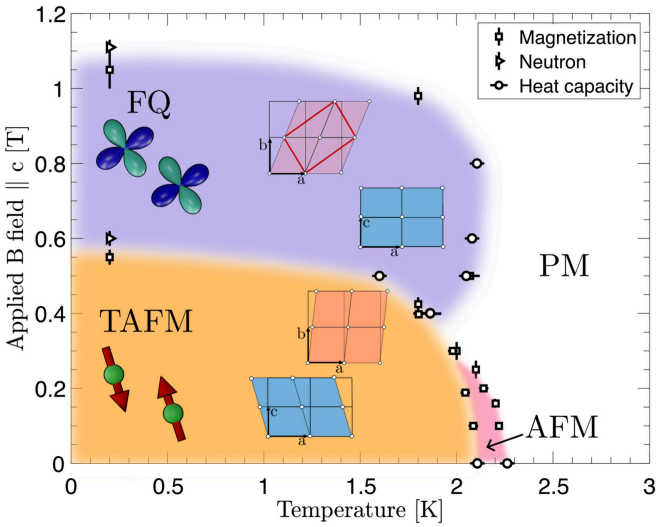

FIG. 1. Magnetic phase diagram for field in the c direction. The phase boundaries are drawn interpolating experimental values from neutron diffraction, heat capacity, and magnetization. Schematic illustrations of the magnetic ordering and the lattice plane deformations within the diagram are shown for each phase. In the TAFM phase, a collinear antiferromagnetic arrangement with magnetic moments tilted away from the c axis is depicted. Both the ac and ab lattice planes exhibit shear deformations, associated with the ε and δ strain components, respectively. In the FQ phase, quadrupolar order is accompanied by an enhanced distortion of the ab plane, while the ac plane distortion disappears. For each type of deformation, only one of the four symmetry-allowed domains is illustrated.

II. QUADRUPOLE INTERACTIONS

We develop a mean-field model which confirms the existence of a pure FQ ordered phase above the magnetic field B_1. In order to relate the observed deformation domains to quadrupole contributions, the x-ray diffraction data are interpreted using a magnetoelastic (ME) Hamiltonian. The model Hamiltonian for the $4f$ magnetic Tb ion in $TbPO_4$ can be written as

$$\mathcal{H} = \mathcal{H}_{\mathrm{CEF}} + \mathcal{H}_{\mathrm{M}} + \mathcal{H}_{\mathrm{ME}} + \mathcal{H}_{\mathrm{E}} + \mathcal{H}_{\mathrm{Q}}. \tag{1}$$

The term $\mathcal{H}_{\mathrm{CEF}}$ describes the crystal electric field and $\mathcal{H}_{\mathrm{M}}$ the combined effect of magnetic dipole interactions and the Zeeman interaction. The details are provided in Appendix A 2.

In the mean-field approximation, the ME term $\mathcal{H}_{\mathrm{ME}}$ describes the direct coupling between the lattice deformation, represented as symmetrized strains e^{μ} ($\mu = \alpha, \delta, \gamma, \varepsilon$, see Appendix A 1), and the $4f$ orbital moments, expressed using Stevens operators. These are combined based on the point group symmetry of Tb ions, resulting in a series of

invariants, each associated with a magnetoelastic coefficient B^μ. Two deformations are particularly relevant for this study. The δ strain corresponds to shear deformations in the xy plane and has B_{2g} symmetry, associated with the Stevens operator $O_2^{-2} = J_x J_y + J_y J_x$. Similarly, the ε strain describes shear deformations in the yz and xz planes, with E symmetry, associated with $O_2^1 = (J_x J_z + J_z J_x)/2$ and $O_2^{-1} = (J_y J_z + J_z J_y)/2$ (a detailed description of the Stevens operators may be found in [23,24]). These contributions to the ME Hamiltonian for a single Tb ion are

$$\mathcal{H}_{\mathrm{ME}}^{\delta,\varepsilon} = -B^\delta e^\delta O_2^{-2} - B^\varepsilon (e_1^\varepsilon O_2^1 + e_2^\varepsilon O_2^{-1}). \tag{2}$$

The complete ME Hamiltonian is presented in (A4). The term $\mathcal{H}_{\mathrm{E}}$ in Eq. (1), is the elastic energy derived from the deformations, and $\mathcal{H}_{\mathrm{Q}}$ includes the terms due to two-site quadrupole-quadrupole interactions.

The minimization of the free energy with respect to the strains leads to equilibrium strains expressed in terms of the quadrupolar operators, $e^\mu = B^\mu \langle \overline{O^\mu} \rangle / c^\mu$, where $\langle \overline{O^\mu} \rangle$ denotes the thermal expectation value of O^μ averaged over all sites, and c^μ is the symmetrized elastic constant per Tb ions. The result is

$$\mathcal{H}_{\mathrm{ME}}^{\delta,\varepsilon} = -G^\delta \langle \overline{O_2^{-2}} \rangle O_2^{-2} - G^\varepsilon [\langle \overline{O_2^1} \rangle O_2^1 + \langle \overline{O_2^{-1}} \rangle O_2^{-1}], \tag{3}$$

with $G^\mu = (B^\mu)^2 / c^\mu$ and an elastic energy $\mathcal{H}_{\mathrm{E}}^{\delta,\varepsilon} = -\langle \mathcal{H}_{\mathrm{ME}}^{\delta,\varepsilon} \rangle / 2$ due to the deformations. As such, the magnetoelastic interactions give rise to indirect quadrupole-quadrupole interactions between different sites mediated by the strains. The quadrupole-quadrupole interaction $\mathcal{H}_{\mathrm{Q}}$ is the sum of electric two-site interactions and the more important quadrupole interactions mediated by acoustic and optical phonons. Within the mean-field approximation, $\mathcal{H}_{\mathrm{Q}}$ may contribute with the same terms as $\mathcal{H}_{\mathrm{ME}} + \mathcal{H}_{\mathrm{E}}$. This implies that the uniform components of the quadrupole-quadrupole interactions in $\mathcal{H}_{\mathrm{Q}}$ are accounted for by replacing the quadrupolar couplings in the magnetoelastic part Eq. (3) by effective ones, i.e.,

$$G^\mu = \frac{(B^\mu)^2}{c^\mu} + K^\mu \quad (\mu = \alpha, \gamma, \delta, \varepsilon), \tag{4}$$

where K^μ is the contribution of the quadrupole-quadrupole interactions in $\mathcal{H}_{\mathrm{Q}}$.

III. EXPERIMENTAL METHODS

Needle-shaped $TbPO_4$ single crystals were grown in a flux of $Pb_2P_2O_7$ at EPFL, following the method described in Appendix B 1. The samples were characterized by heat capacity and x-ray measurements.

To study the deformation of the crystal structure as a function of magnetic field and temperature, we performed an x-ray diffraction experiment at the P09 beamline at PETRA III using a He-3 insert [25] and a 14 T vertical field cryomagnet to investigate the desired $(\mu_0 H, T)$ region of the phase diagram. A 5.3 mg $TbPO_4$ single crystal ($2.1 \times 1.3 \times 0.5$ mm^3) was polished with 0.25 μm diamond paste and mounted on a copper oxygen free holder using GE varnish and silver paint to improve thermal contact. It was oriented with the crystallographic c axis vertical, along the magnetic field direction and $\boldsymbol{Q} = (HK0)$ in the scattering plane. As verified with a Laue camera, the vertical angle offset was less than 1°. The incident x-ray beam had a fixed energy of 27 keV. Beam attenuation was required to avoid sample heating. The experiment was performed in reflection geometry. A Pilatus area detector with a pixel resolution of 0.015°/pixel was used to collect the integrated intensity of photons diffracted from the sample as a function of sample rotation around the horizontal (ω) axis. We monitored four Bragg reflections: (20, 0, 0), (20, 2, 0), (14, 6, 0), (16, 8, 0), and (13, 8, 1).

Neutron diffraction data were collected on the ZEBRA diffractometer at PSI using a 6 T vertical field cryomagnet with a dilution insert. A $TbPO_4$ single crystal with mass of 39.4 mg was mounted on an aluminum oxygen free plate using low temperature epoxy, with $\boldsymbol{Q} = (HK0)$ in the horizontal plane and the c axis vertical. The wavelength of the incident neutrons were selected by Ge(311) ($\lambda = 1.177$ Å) or PG(002) ($\lambda = 2.317$ Å) monochromators. Slits were used to limit the beam divergence. The scattered neutrons were recorded using a 2D detector for efficient reciprocal space mapping or a 1D detector for higher resolution data.

In addition, we investigated macroscopic quantities such as magnetization and heat capacity. The field dependence of the magnetization was measured at EPFL (LQM laboratory) using a Cryogenic SQUID with a He3 insert. The $TbPO_4$ crystal was 3 mg, mounted on a quartz holder using GE varnish. Heat capacity measurements were performed using a PPMS with a He3 insert at Helmholtz-Zentrum Berlin on a 2 mg $TbPO_4$ single crystal, with a dimension of approximately $1.5 \times 0.8 \times 0.4$ mm^3.

IV. RESULTS

A. Measurement of uniform strain symmetry

Using x-ray diffraction, we identify the structural distortions associated with the symmetry of the observed peak splittings.

The combination of a 2D detector and sample rotation through the Bragg peak allows us to measure a 3D map of reciprocal space in its vicinity, enabling a comprehensive analysis of the peak splitting. To study the strains in the zero field AFM phase, we study the behavior of (14, 6, 0) and (20, 0, 0) Bragg peaks as a function of temperature. Concerning the basal plane, Fig. 2(a) (I) shows 2D intensity distribution in HK reciprocal plane of the (14, 6, 0) Bragg peak. The peak splits into four distinct domains in the

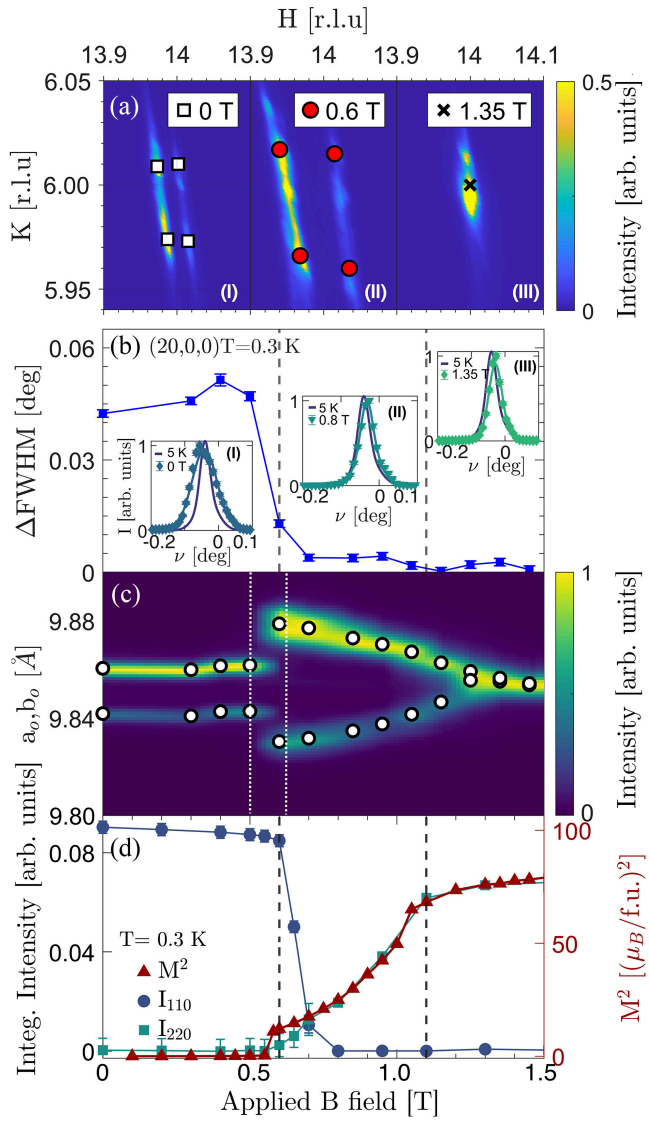

FIG. 2. (a) (14,6,0) Bragg peak at 0.3 K for an external field of 0 T (I), 0.6 T (II), and 1.35 T (III). The markers represent the simulated position of the different domains deriving from the δ strain. (b) Field dependence of ΔFWHM of (20, 0, 0) Bragg peak at 0.3 K. Inset: peak shape as a function of vertical scattering angle ν at 0.3 K for external field of 0 T (I), 0.8 T (II), 1.35 T (III). Solid lines are Gaussian fit. The peak at 5 K is shown as a reference for the undeformed case. (c) Integrated intensity of the $(14, 6, 0)_T$ peak versus applied magnetic field. White dots represent the field dependence of the lattice parameters a_O and b_O. Dashed white lines highlight the region of coexistence. (d) Neutron diffraction data. Left y axis: Lorentz corrected integrated intensities (magnetic contribution only) for AFM (1, 1, 0) and FM (2, 2, 0) Bragg peaks as a function of the applied magnetic field. The solid lines serve to aid visualization. Right y axis: red markers show the square of the magnetization measurement at $T = 30$ mK.

low-temperature phase, below T_S. By simulating the structural distortion, shown by markers in Fig. 2(a)(I), we uniquely identify the deformation to be a δ strain of symmetry B_{2g}. Details of the simulation methodology are provided in Appendix B 3. The ME Hamiltonian (2) implies that the observation of the δ strain deformation in the zero-field AFM phase at 0.3 K has the consequence that the δ quadrupole moments are uniformly ordered, $\langle \overline{O_2^{-2}} \rangle = e^{\delta} c^{\delta} / B^{\delta}$.

The out-of-plane deformation is detected by examining the (20, 0, 0) Bragg peak in the HL plane. The inset (I) in Fig. 2(b) compares the peak profile at 0.3 K with the one at 5 K as a function of the vertical scattering detector angle ν. The scattering profile at 0.3 K, below T_S, is significantly broader than the one at 5 K indicating an additional distortion. Based on the symmetrized strains allowed in the tetragonal structure, we identify this deformation to be an ε strain, that is a shear distortion of the ac lattice plane (see Appendix A 1, Table I). The ε strains being nonzero imply that the $\langle \overline{O_2^{\pm 1}} \rangle$ quadrupole moments are nonzero and establish an additional quadrupole ordering in the AFM dipolar phase.

To investigate the strains in the field-induced phase, we track the evolution of the strains ε and δ. The ε strain can be examined based on the evolution of the broadening of the (20, 0, 0) peak in the vertical plane, defining ΔFWHM as the difference between the peak width at low temperature and the width of the undeformed peak at high temperature.

Figure 2(b) shows that the peak broadening disappears when entering the intermediate field phase at 0.6 T, determining the complete disappearance of the ε strain in this phase. This indicates that the lattice angle β is restored to the 90°—the value in the tetragonal structure—by the application of a magnetic field, and, therefore, that the two quadrupolar order parameters $\langle \overline{O_2^{\pm 1}} \rangle$ are zero both in the intermediate field phase and in the phase appearing above B_2.

In the basal plane on the other hand, the effect of the magnetic field is more significant. The x-ray results in Fig. 2(a)(II) show that the separation between the domains at 0.3 K is increased drastically at 0.6 T compared to the zero field case. The simulation confirms that the B_{2g} symmetry is retained at 0.6 T, establishing the presence of the δ strain and a large contribution of the O_2^{-2} quadrupoles at this field. At 1.35 T, Fig. 2(a)(III), only a single scattering peak remains as in the paramagnetic case at 5 K.

Given the crucial contribution of the δ strain in the intermediate field-induced phase, we propose that the symmetry lowering of the crystal lattice defines a new orthorhombic unit cell, shown in red in the sketch in Fig. 1

with lattice parameters a_O and b_O. Figure 2(c) shows the field dependence of these lattice parameters and the integrated intensity of the reflection $(14, 6, 0)_T$. At the phase boundary at B_1, the co-existence of the phases indicates a first-order phase transition, resulting in a symmetry lowering to the $Fddd$ space group. The δ quadrupolar ordering decreases gradually as the field is increased further above 0.6 T and vanishes at the transition (probably of second order) to a phase at 1.1 T with no quadrupole order, i.e., the paramagnetic phase. Having established the strain and therefore the quadrupolar components in the (H, T) phase diagram, we proceed to investigate the magnetic order parameter.

B. Absence of antiferromagnetic order in the intermediate field region

We measure the (1, 1, 0) and (2, 2, 0) Bragg reflections using neutron diffraction. Evaluation of the nuclear and magnetic structure factors for the (1, 1, 0) and (2, 2, 0) Bragg peaks show that the former only reflect the antiferromagnetic order, while the latter has a weak nuclear contribution in addition to a signal deriving from the ferromagnetic order. To isolate the ferromagnetic contribution to (2, 2, 0), the nuclear component measured at $T > T_N$ was fitted and subtracted from the data obtained in the ordered state. Figure 2(d) shows the field dependence of the integrated intensities after correction for the Lorentz factor, considering only their magnetic components.

The AFM (1, 1, 0) reflection is characteristic of the zero-field AFM order and rapidly decreases to zero as the magnetic field value crosses the phase boundary at B_1. This behavior is consistent across all observed AFM Bragg peaks. Parallel to the disappearance of the AFM signal, we detect a progressive increase in the FM contribution, revealed by the increase of the integrated intensity of the (2, 2, 0) reflection with increasing magnetic field. This growth is consistent with the square of the bulk magnetization M^2, as measured by SQUID magnetization, see Fig. 2(d). Therefore, the FM neutron cross section scales with the square of the field, and thus the peak intensity increase derives solely from the field-induced FM components.

Using a 2D neutron detector we probe an h, k range up to 2 r.l.u. and l range of ± 1 r.l.u.. No sign of multiple-k order or incommensurate order were found above B_1 and no additional AFM Bragg peak was discovered (see Appendix B 2). Hence, the absence of any magnetic scattering beyond the established magnetic peaks in this intermediate phase suggests that a spin-flop transition is unlikely.

From neutron and x-ray data, we identify the intermediate phase as being dominated by the O_2^{-2} quadrupolar term, leading to the emergence of ferroquadrupolar order. To further explore this phase, we measure the heat capacity (HC) within the FQ region.

C. Heat capacity of the ferroquadrupolar phase

Figure 3(a) shows the temperature dependence of the heat capacity HC between 0.4 and 3.8 K in the zero-field phase and the intermediate field region.

At zero field, two sharp peaks in the HC curve indicate consecutive second-order phase transitions. At 0.8 T there is only the one transition to the intermediate phase detected at 2.1 K, and in this phase, the HC exhibits an approximately linear decrease below the critical temperature, contrasting with the low-field behavior ($B < B_1$). Although a conventional spin-flop transition would typically produce a lambda anomaly associated with the AFM ordering, the observed HC behavior deviates from this expectation. Instead, the gradual, quasilinear decrease is reported to be a characteristic feature of the cooperative Jahn-Teller-like FQ phases in $TmVO_4$ [9] and $TmAg_2$ [8].

The calculated curves based on the mean-field approximation [see Fig. 3(b)] are in qualitative agreement with the experimental data. The model does not contradict the experimental observation that the heat capacity decreases relatively slower in the quadrupolar-ordered phase than in the antiferromagnetic case.

V. DISCUSSION

Our neutron and synchrotron x-ray diffraction data show only one strain above B_1 and no dipolar magnetic order, besides the field-induced magnetization. This is extraordinarily consistent with the mean-field results, shown in Fig. 4, where only O^δ is the nontrivial order parameter.

In zero field, however, the nature of the magnetic order in the model is exceedingly complex, which is indeed observed experimentally, where we establish two distinct strains via direct observation: the basal plane δ strain (also determined by Nägele *et al.* [26]) and the monoclinic ϵ strain. Since these strains are directly coupled to the expectation values of quadrupolar operators [Eqs. (2) and (3)], we have identified a remarkably complex

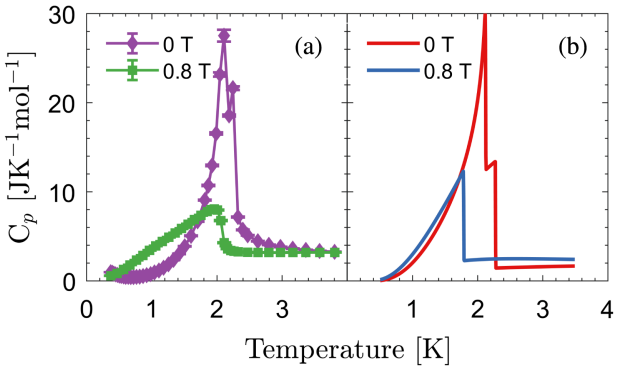

FIG. 3. (a) Heat capacity curves as a function of temperature at 0 and 0.8 T, displaying the different temperature dependence of the curves in the two distinct phases. (b) Heat capacity curves at 0 and 0.8 T calculated from the mean-field model.

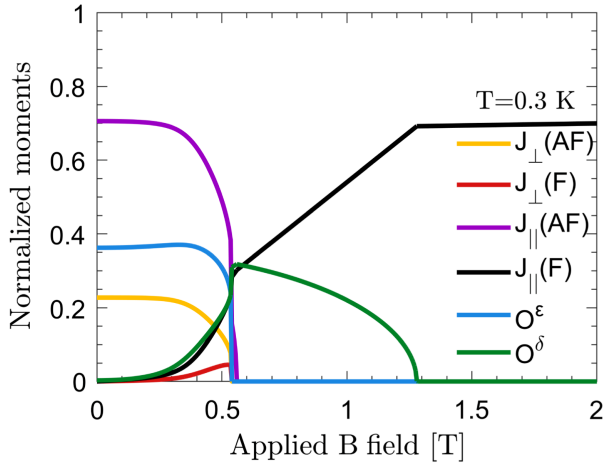

FIG. 4. The calculated normalized dipole and quadrupole moments at 0.3 K as a function of applied magnetic field along the c axis. $J_{\parallel}[(A)F]$ and $J_{\perp}[(A)F]$ are the components of the (anti) ferromagnetic angular moment, divided by $J = 6$, respectively parallel and perpendicular to the c axis. O^{δ} shows the calculated result of $\langle\overline{O_2^{-2}}\rangle/33$, and O^{ε} is $[\langle\overline{O_2^{1}}\rangle^2 + \langle\overline{O_2^{-1}}\rangle^2]^{1/2}/16.5$. The model used in the mean-field calculations is presented in Appendix A 2.

magnetic ground state, involving tilted AFM coexisting with two distinct quadrupolar orderings (O_2^{-2} and $O_2^{\pm 1}$).

In particular, our detection of the out-of-plane monoclinic distortion shows the ε strain to be $e_{xz} = 0.52 \times 10^{-3}$ at zero field at 0.3 K, a factor of 2 higher than previously reported [19], corresponding to a tilting of the c axis by an angle $\Delta\beta = 2e_{xz} = 0.06°$. Using $c^{\varepsilon} \simeq 6.7 \times 10^4$ meV per Tb-ion [19], the magnetoelastic contribution $G^{\varepsilon}_{\mathrm{ME}}$ is found to be $\simeq$1.0 μeV, one-quarter of the effective value of G^{ε} derived in Appendix A 2. In the mean-field model, the transition to the tilted antiferromagnet at T_S is exclusively driven by the ε quadrupole interaction, and we expect that our mean-field analysis gives a quite precise determination of G^{ε}. Being proportional to the square of the strain the uncertainty of the estimate of the magnetoelastic contribution to G^{ε} is rather large, nevertheless the quadrupolar interaction, K^{ε}, is found to be the dominating term in G^{ε}.

The application of an external magnetic field suppresses the complexities of the zero-field AFM phase, inducing a transition to the FQ ordered phase at $B_1 = 0.6$ T. A tilting of the ordered magnetic moment away from the c axis will always be accompanied by a nonzero ε strain, and the absence of an ε strain in the intermediate phase indicates that $\langle\overline{O_2^{-2}}\rangle$ is the only order parameter left in this phase. Our neutron diffraction investigations lead to the same conclusion, which is further substantiated by the result of our heat capacity measurements. Hence our x-ray and neutron diffraction results rule out the previously proposed spin-flop scenario [27,28].

The results in Fig. 2(b) show that the maximum δ strain is $e_{xy} = (a_O - b_O)/(a_O + b_O) = 2.1 \times 10^{-3}$ at 0.6 T. The $TbPO_4$ crystal is soft with respect to a δ strain deformation, and the elastic constant is estimated to be $c^{\delta} \simeq 1.8 \times 10^4$ meV [19], nearly a factor of 4 smaller than c^{ε}. The magnetoelastic contribution to G^{δ} determined by these results is $G^{\delta}_{\mathrm{ME}} = 1.3$ μeV, which is just the value of G^{δ} derived in the mean-field analysis. From their studies of the paramagnetic strains Morin *et al.* [19] determine the effective δ contribution to be $G^{\delta} = 1.5$ μeV. This value is close to the present result and only slightly smaller than the critical value—estimated to be about 1.65 μeV in the mean field calculations—above which the FQ-ordered phase dominates and effectively prevents any antiferromagnetic ordering of the moments.

The surprising observation of a field-induced ferroquadrupolar order therefore reflects the fact that $TbPO_4$ is on the verge of being fully dominated by quadrupolar couplings: increasing the coupling constant G^{δ} by about 25% would entirely suppress the dipolar antiferromagnetic order, leaving a phase diagram with quadrupolar order below the critical field of 1.5 T. In $TbPO_4$, the magnetic interactions remain large enough to produce a complex spontaneous AFM ground state, which is suppressed by a critical c-axis field of 0.6 T. This critical field is not much affected by the G^{δ} coupling, as long as it is smaller than the critical value. Note that the role of the magnetic field is not to create a magnetoelastic coupling leading to quadrupolar order (it is already present at zero field, as seen in Fig. 4), but rather to suppress antiferromagnetic order, leaving only the δ-type ferroquadrupolar order above 0.6 T. The tendency of the system to ferroquadrupolar order is a combination of a very soft ab plane [17], combined with a crystal field level scheme susceptible to the creation of quadrupole moments O_2^{-2}.

The estimate of the interaction parameter G^{δ}_{ME} indicates that this magnetoelastic contribution is the dominating one, $K^{\delta} \simeq 0$, in strong contrast to the behavior of the ε quadrupole-quadrupole interaction. Moreover, the CEF level scheme of the Tb ions has a doublet as ground state with a moment $\langle J_z\rangle/J \simeq 0.69$. The mean-field model predicts, see Fig. 4, that the antiferromagnetic moment at zero field is close to the ground-state saturation value.

The field-induced δ strain is equivalent to an electrical quadrupolar shift of the charge distribution around the Tb^{3+} ions, giving rise to the magnetic quadrupolar moment $J_xJ_y + J_yJ_x = O_2^{-2}$, and thus establishes a collective magnetostructural order parameter. The FQ order is a unique form of electronic nematicity that in the $4f$ system realizes an Ising nematic order, where rotational symmetry—in this case the C_4 rotational symmetry—is broken, while translational symmetry is preserved. Systems exhibiting nematic order often share universal scaling behavior and play a key role in the study of quantum critical phenomena [29]. In general, the tunability of FQ order via external fields allows detailed investigations of the critical nematic fluctuations

near a quantum critical point, as exemplified by the case of $TmVO_4$ in Ref [9].

Deepening our understanding of the nematic phase transition in model systems can bring insight into more complex materials, where nematicity is only one of several nearly degenerate order parameters. For example, the coexistence and interplay of nematicity and antiferromagnetic order is realized in the iron pnictides, where an electronic nematic instability, driven by anisotropic spin fluctuations or orbital polarization modifies and often precedes antiferromagnetism, and this interaction is linked to the superconducting coupling mechanism [30,31]. Examples include $BaFe_2As_2$ and its K-doped derivatives $Ba_{1-x}K_xFe_2As_2$ [32,33], as well as $FeSe_{1-x}Te_x$ [34], which together highlight the coupled nature of nematicity, magnetism, and unconventional superconductivity. Similarly, quadrupolar order is relatively common in rare-earth heavy-fermion systems and has been shown to precede or coexist with superconductivity as in YbAs [35,36] and PrV_2Al_{20} [37,38].

As model systems for pure nematic phase transitions, $TmVO_4$ [9] and $YbRu_2Ge_2$ [39] have been extensively studied, due to the simple ferroquadrupolar phase diagrams, resulting from the dominance of the quadrupole-quadrupole interaction over any exchange terms. In $TbPO_4$, on the other hand, the ferroquadrupolar and antiferromagnetic states are energetically nearly degenerate, and the order parameters coexist in the ground state. Thus, $TbPO_4$ offers a more versatile testing ground for phase transitions involving nematicity, as a weak first order transition between nematic and magnetic phases can be studied in addition to the second order quantum critical point that separates the FQ and paramagnetic phases, in the same material. In particular, investigating soft mode behavior and domain wall physics at the magnetic-nematic transition are promising next steps. Within the rare earth zircon family, field induced ferroquadrupolar order has been predicted to occur between 10 and 60 T in $TmPO_4$ [40], between 50 and 250 T in $YbVO_4$ [41] and above 150 T in $YbPO_4$ [42]. Among these other members of the rare earth zircon family, $TbPO_4$ stands out by having full access to the nematic-ferroquadrupolar and antiferromagnetic phase diagram within experimentally accessible magnetic fields.

Experimentally, the presented methodology uses direct measurements of the full domain-induced peak splitting with high-resolution position-sensitive x-ray detectors to uniquely identify the symmetrized strain and, consequently, the symmetry of the ordered quadrupole moment. This approach can be widely utilized to resolve magnetoelastic Hamiltonians in other compounds. The unambiguous determination of the magnetoelastic Hamiltonian is crucial in modeling the phonon-mediated coupling between quadrupoles, enabling a better understanding of related complex phenomena, such as piezomagnetism in uranium dioxide [43] and ferroquadrupolar domain switching in $Pb(TiO)Cu_4(PO_4)_4$ [44].

Regarding the magnetoelectric effect, Bluck *et al.* [17] linked the magnetoelectric coupling in $TbPO_4$ to polar distortions of the crystal field, driven by the cooperative Jahn-Teller effect. However, the lack of experimentally tuned parameters for the mean-field Hamiltonian led to discrepancies with observations. Many other members of the rare-earth zircon phosphates and vanadates are magnetoelectric [45], but with 1–2 orders of magnitude weaker couplings, and the underlying cause for the extremely strong ME coupling in $TbPO_4$ specifically has yet be understood. The understanding of the full magnetoelastic Hamiltonian presented here is essential for modeling the softening of the low-energy magnetoelastic dynamics, potentially enhancing the magnetoelectric response.

VI. CONCLUSION

We have revealed the existence of field-induced hidden order in magnetoelectric $TbPO_4$. Using synchrotron x-ray diffraction, neutron diffraction, heat capacity, and mean-field modeling, we have, via the measurement of uniform strain, identified the specific symmetry of the ordered quadrupoles to be O_2^{-2}. The footprints of the field-induced FQ order are seen consistently across the various techniques. Additionally, our x-ray diffraction measurements identify a complex ground state, with tilted dipolar antiferromagnetism co-existing with two distinct ferroquadrupolar orders ($O_2^{\pm 1}$ and O_2^{-2}, respectively). This complex magnetoelastic phase diagram has enabled a comprehensive understanding of the magnetoelastic Hamiltonian, providing a robust framework for modeling the intricate interplay of magnetoelastic and magnetoelectric couplings within this family of rare-earth zircon magnets.

ACKNOWLEDGMENTS

The work was supported by the Danish national Committee for Research Infrastructure (NUFI) through the ESS-Lighthouse Q-MAT and by a research grant (Grant Agreement No. 35921) from VILLUM FONDEN. This project has received funding from the Swiss National Science Foundation (SNSF) under Grant No. 200020-188648 and from the European Research Council (ERC) under the European Union's Horizon 2020 research and innovation program (Grant Agreement No. 810451). The experimental work was supported by the instrument center DanScatt funded through the Danish Agency for Science, Technology, and Innovation through Grant No. 7129-00006B. We acknowledge DESY (Hamburg, Germany), a member of the Helmholtz Association HGF, for the provision of experimental facilities. Parts of this research were carried out at PETRA III at DESY. Beamtime at P09 was allocated for proposal I-20210985 EC. The neutron diffraction experiments were performed on ZEBRA at the Swiss spallation neutron source SINQ, Paul Scherrer Institute, Villigen, Switzerland. We acknowledge the use

of the Physical properties laboratory, which is part of the CoreLab "Quantum Materials" operated by Helmholtz-Zentrum Berlin.

DATA AVAILABILITY

The data that support the findings of this article are openly available [46], embargo periods may apply.

APPENDIX A: THE MEAN-FIELD MODEL

1. The symmetrized strains

The theory describing the uniform strains in the crystal is based on the *symmetrized strains* [47]. These are linear combinations of the infinitesimal strains that account for the D_{4h} point group symmetry of $TbPO_4$ and they are reported in Table I. The δ strain refers to a e_{xy} shear deformation of the basal plane while ε strain represents a $e_{xz/yz}$ shear deformation of the ac/bc lattice plane. As reported in the table, each strain is associated with an irreducible representation of the crystallographic point group.

2. The magnetic Hamiltonian

The mean-field Hamiltonian applied in the present analysis of the magnetic properties of $TbPO_4$ is qualitatively close to the one presented by Morin *et al.* [19]. Like in this article the x, y, and z axes are chosen to be along the a, b, and c axes, respectively. The crystal electric field (CEF) Hamiltonian of a single Tb ion is

$$\mathcal{H}_{\mathrm{CEF}} = \sum_{l=2,4,6} B_l^0 O_l^0 + \sum_{l=4,6} B_l^4 O_l^4. \tag{A1}$$

The parameters are derived by a least-square fitting of the experimental CEF level scheme determined by Bohm *et al.* [48] at 4.2 K, and are [in units of meV]:

$$B_2^0 = -0.225, \quad B_4^0 = 0.387\times10^{-3}, \quad B_6^0 = 0.494\times10^{-5},$$
$$B_4^4 = 0.135\times10^{-1}, \quad B_6^4 = -0.67\times10^{-5}. \tag{A2}$$

When including the magnetoelastic α contribution (see below) the effective B_2^0 is -0.231 meV at 4.2 K. These crystal-field parameters are nearly the same as presented in Table II (Set 2) of Ref. [19].

The total magnetic Hamiltonian, $\mathcal{H}_{\mathrm{M}}(i)$ in Eq. (1), is the Zeeman term $-g\mu_B \mathbf{J}\cdot\mathbf{H}$ plus the two-ion interactions $-\frac{1}{2}\sum_j \sum_{\alpha\beta} \mathcal{J}^{\alpha\beta}(i,j) J_i^\alpha J_j^\beta$, which are considered to be the sum of an isotropic Heisenberg exchange and the classical dipole-dipole interaction. A basic assumption is that the ordered structures may all be described in terms of two sublattices, the body-centered tetragonal lattices centered at (0, 0, 0) and at $(a/2, 0, c/4)$. This means that we only need to specify the Fourier components of the total two-ion interactions at the reciprocal lattice vectors 0 and $\boldsymbol{Q} = (0, 0, 2)$, and that only the diagonal components, $\alpha\beta = aa$ or cc, are nonzero. By fitting the Néel temperature $T_N = 2.28$ K and the paramagnetic susceptibility components [19] we get [in units of meV]:

$$\mathcal{J}^{cc}(\boldsymbol{Q}) = 0.0115, \quad \mathcal{J}^{aa}(\boldsymbol{Q}) = \mathcal{J}^{cc}(\boldsymbol{Q}) - 0.0047,$$
$$\mathcal{J}^{cc}(\mathbf{0}) = -0.018, \quad \mathcal{J}^{aa}(\mathbf{0}) = \mathcal{J}^{cc}(\mathbf{0}) + 0.0043, \tag{A3}$$

where the anisotropy is a consequence of the classical dipole-dipole interaction.

The magnetoelastic interactions appear because any deformation of the lattice is going to change the crystal field acting on the $4f$ orbitals of the Tb ions. The terms allowed by symmetry are the products of the different symmetrized strains e^μ in Table I and the Stevens operators, which both transform according to the same irreducible representation of the D_{4h} point group. Each invariant is associated with a ME coefficient B^μ and the single-ion ME term is

$$\mathcal{H}_{\mathrm{ME}} = -(B^{\alpha1}e^{\alpha1} + B^{\alpha2}e^{\alpha2})O_2^0 - B^\gamma e^\gamma O_2^2 - B^\delta e^\delta O_2^{-2} - B^\varepsilon(e_1^\varepsilon O_2^1 + e_2^\varepsilon O_2^{-1}). \tag{A4}$$

If it is energetically favorable, the crystal may deform without applying an external stress. This may occur

TABLE I. Symmetrized strains and elastic constants for each representation (Repr.) of the D_{4h} crystal point group, adapted from [19].

Repr.	Strains	Elastic constants
A_1	$e^{\alpha1} = \frac{1}{\sqrt{3}}(e_{xx}+e_{yy}+e_{zz})$	$c^{\alpha1} = \frac{1}{3}(2c_{11}+2c_{12}+4c_{13}+c_{33})$
A_1	$e^{\alpha2} = \sqrt{\frac{2}{3}}[e_{zz} - \frac{e_{xx}+e_{yy}}{2}]$	$c^{\alpha12} = -\frac{\sqrt{2}}{3}(c_{11}+c_{12}-c_{13}-c_{33})$
		$c^{\alpha2} = \frac{1}{3}(c_{11}+c_{12}-4c_{13}+2c_{33})$
B_{1g}	$e^\gamma = (e_{xx}-e_{yy})/\sqrt{2}$	$c^\gamma = c_{11}-c_{12}$
B_{2g}	$e^\delta = \sqrt{2}e_{xy}$	$c^\delta = 2c_{66}$
E	$e_1^\varepsilon = \sqrt{2}e_{zx}$	$c^\varepsilon = 2c_{44}$
	$e_2^\varepsilon = \sqrt{2}e_{yz}$	

spontaneously or as a response to a magnetic field, and the equilibrium strains minimizing the free energy are straightforwardly determined to be $e^{\mu} = B^{\mu}\langle\overline{O^{\mu}}\rangle/c^{\mu}$ ($\mu = \gamma, \delta, \varepsilon$), for details see Refs. [11,24]. The result in the case of $\mu = \alpha$ may be found in Ref. [19]. Introducing the equilibrium strains in the mean-field Hamiltonian we get

$$\begin{aligned}\mathcal{H}_{\mathrm{ME}} + \mathcal{H}_{\mathrm{E}} = &-G^{\alpha}\langle\overline{O_2^0}\rangle O_2^0 - G^{\gamma}\langle\overline{O_2^2}\rangle O_2^2 - G^{\delta}\langle\overline{O_2^{-2}}\rangle O_2^{-2} \\ &- G^{\varepsilon}[\langle\overline{O_2^1}\rangle O_2^1 + \langle\overline{O_2^{-1}}\rangle O_2^{-1}] \\ &+ \frac{1}{2}G^{\alpha}\langle\overline{O_2^0}\rangle^2 + \frac{1}{2}G^{\gamma}\langle\overline{O_2^2}\rangle^2 + \frac{1}{2}G^{\delta}\langle\overline{O_2^{-2}}\rangle^2 \\ &+ \frac{1}{2}G^{\varepsilon}[\langle\overline{O_2^1}\rangle^2 + \langle\overline{O_2^{-1}}\rangle^2]. \qquad \text{(A5)}\end{aligned}$$

The magnetoelastic strain contributions appear effectively in the Hamiltonian like those deriving from the uniform quadrupole-quadrupole interactions. Consequently, the uniform contributions of $\mathcal{H}_{\mathrm{Q}}$ are accounted for by adding the quadrupole-quadrupole contribution, K^{μ}, to the strain dependent part of G^{μ}, see Eq. (4). The quadrupole moments on the two sublattices differ from each other, $\langle O_2^m\rangle(i) \neq \langle\overline{O_2^m}\rangle$, only when the c-axis field is nonzero but smaller than B_1. The results derived in this field interval are found to depend only weakly on whether the δ and ε contributions originate from the strains or from nearest neighbor quadrupole-quadrupole interactions. In the latter case, the transition field B_1 is reduced from 0.54 to 0.45 T. This difference is exclusively due to the δ contribution, which is most likely a pure strain term. Hence, the nonuniform parts of $\langle O_2^m\rangle(i)$ are of no importance for the ground state properties, but might lead to dispersion effects on the excitations.

The last parameters in the mean-field model are the effective values of the four coupling parameters G^{μ}, and they are [in units of μeV]:

$$G^{\alpha} = 0.215, \quad G^{\gamma} = 0.9, \quad G^{\delta} = 1.28, \quad G^{\varepsilon} = 4.15. \qquad \text{(A6)}$$

G^{ε} is responsible for the tilting of the antiferromagnetic moments away from the c axis below T_S and is determined by requiring $T_S = 2.13$ K. The other important parameter G^{δ} is adjusted so as to get agreement with the transitions observed in the c-axis field at 0.3 K. The two remaining parameters have some influences on the calculated results, but in these two cases we have simply used the values estimated by Morin *et al.* [19].

3. Results from the mean-field model

The results of the mean-field model shown in Fig. 4 are in good agreement with our experiments in an applied c-axis field up to 1.5 T at 0.3 K. The only significant discrepancy is that the X-ray experiment shows $e_{xy} \simeq 0.9 \times 10^{-3}$ at zero field, see Fig. 2(b), whereas the model predicts that the δ strain becomes very small and nearly vanishes in the zero field limit. Extending the calculations to higher fields we get the results shown in Fig. 5. The mean-field model predicts the unusual behavior that the simple paramagnet appearing above 1.1 T is going to be interrupted by a new ordered phase between about 2 and 10 T. In this phase the paramagnetic moment along the c axis has a ferromagnetic ordered component perpendicular to the field and both the ε and the δ strains are nonzero. The presence of a magnetic moment along the z axis affects the $O_2^{\pm 1}$ quadrupoles so that they effectively contribute to the dipole interactions between the (x, x) and (y, y) components. This mechanism is responsible for the appearance of the simultaneous ordering of the moments in the (xy) plane and the ε quadrupoles at a temperature T_S below T_N, where the c-axis moments have grown to be sufficiently large. The dominance of the δ quadrupole interactions within the (xy) plane then makes $\langle 1, 1, 0\rangle$ the preferred directions for the tilted moments. These same observations explain the appearance of the extra field-induced phase, and, clearly, further investigations at the higher magnetic field needs to be conducted to confirm this surprising possibility.

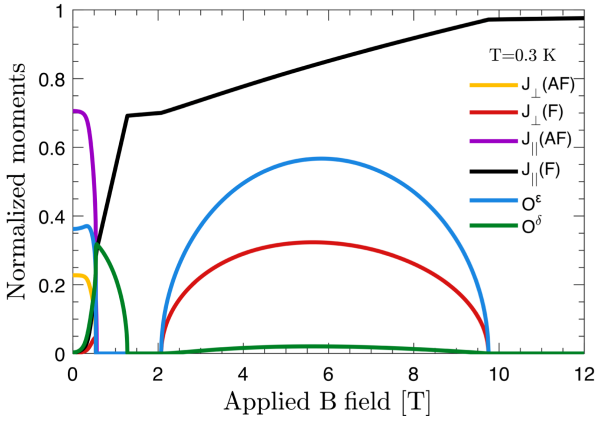

FIG. 5. Normalized dipole and quadrupole moments at 0.3 K as a function of applied field along the c axis. The symbols used are defined in Fig. 4.

APPENDIX B: SUPPLEMENTAL MATERIAL ON THE EXPERIMENTAL DATA

1. Growth of $TbPO_4$ single crystals

$TbPO_4$ single crystals were grown using a $Pb_2P_2O_7$ flux [49–51]. The first step was the synthesis of $TbPO_4$ powder. $TbCl_3$ powder was added to a dilute H_3PO_4 solution while the mixture was rapidly stirred to dissolve the $TbCl_3$. The solution was kept in a fume hood for three days, during which a white powder of $TbPO_4 nH_2O$ gradually precipitated. This powder was collected using filter paper, washed with distilled water, and then calcined in a furnace at 1100 °C for 6 h. X-ray diffraction measurements confirmed the formation of pure $TbPO_4$.

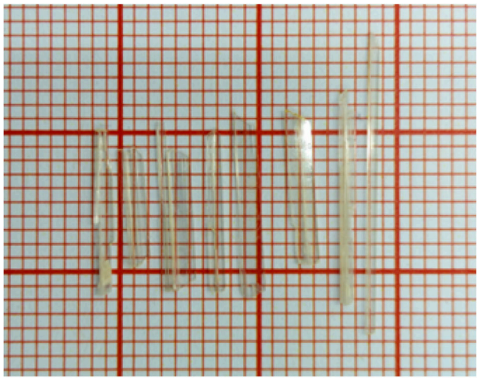

FIG. 6. The needlelike $TbPO_4$ single crystals grown from the $Pb_2P_2O_7$ flux.

The $Pb_2P_2O_7$ flux was synthesized by heating a mixture of $PbCO_3$ and $(NH_4)H_2PO_4$ at 700°C for 12 h. The resulting flux was then mixed with the $TbPO_4$ powder at a 1:19 molar ratio in a platinum (Pt) crucible. The crucible was heated to 1350 °C, held at that temperature for 12 h, and then slowly cooled down to 800 °C at a rate of 2 °C/h. Needlelike single crystals formed during this cooling process.

To separate the crystals from the flux, the Pt crucible was immersed in a diluted HNO_3 solution and heated to 80 °C. After 24 h, the needlelike single crystals were successfully separated, as shown in Fig. 6.

2. Investigation of the magnetic phase

The neutron diffraction data collected at ZEBRA (PSI) demonstrate the absence of a full dipole magnetic signal in the intermediate field range between 0.6 and 1.1 T. In addition to the magnetic Bragg peak shown in Fig. 2(c), we measured other reflections. These have non-zero nuclear and (anti)ferromagnetic structure factors. Figure 7 shows the magnetic field dependence of the integrated intensity,

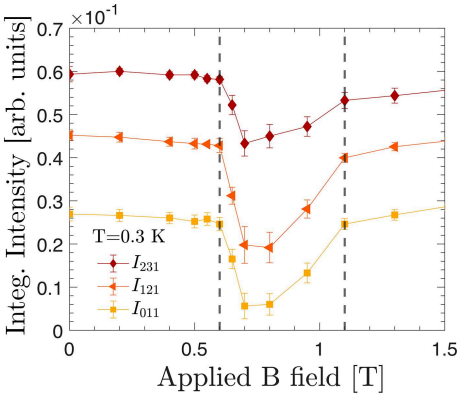

FIG. 7. Magnetic field dependence of the integrated intensities for relevant Bragg peaks. The solid lines serve as guides to the eye. Lorentz correction is considered. Dashed vertical lines highlight the intermediate field region.

TABLE II. Comparison between experimentally observed (Obs) and calculated (Calc) values of the structural intensities at 0.8 T.

	Obs	Calc
I_{121}/I_{231}	0.45 ± 0.12	0.43
I_{011}/I_{231}	0.13 ± 0.07	0.15
I_{031}/I_{231}	1.44 ± 0.23	1.27

decreasing at B_1 for all Bragg peaks. At $\mu_0 H = 0.8$ T, the intensity value is consistent with the nuclear structure factor as listed in Table II, where the observed data are compared with calculations. For accurate intensity comparisons, the Lorentz factor, $[\sin(2\theta)]$, was applied to each sample rotation scan (ω scan). Consequently, there is no indication of any antiferromagnetic (AFM) contribution for the propagation vector $\mathbf{q} = (0, 0, 0)$.

The absence of a dipole magnetic moment is further confirmed by our examination using a two-dimensional position-sensitive detector, which enabled the investigation of Bragg peaks across a broader region of reciprocal space. This analysis leads to the conclusion that there are no discernible AFM peaks, whether commensurate or incommensurate in the intermediate field region. Specifically, the absence of the (2, 2, 1), (2, 1, 0), and (1, 1, 1) peaks excludes the possibility of a magnetic commensurate structure different from that observed at zero field. The incommensurate signal was studied through hkl scans at various positions in Q space, covering a range of $\mathbf{q} = (h, k, l)$ values. Here, h and k were varied from 0 to 2 reciprocal lattice units in steps of 0.5 r.l.u., while l ranged from 0 to 1 r.l.u. in steps of 0.25 r.l.u.

3. Strain simulation

The strain characterizing the field-induced phase transition resembles a δ-type distortion, manifesting as an amplification of the zero-field case. To verify this hypothesis, we simulate the effect of this distortion on the peak positions. These simulations are performed using ISODISTORT [52], which allows us to generate the distorted structure starting from the tetragonal space group $I4_1/amd$. During the generation of the distorted structure, we vary the amplitude of the strain to regulate its impact on the parent structure. Once the distorted structure is determined, we use the Single Crystal module in Crystal Maker software [53] to compare the parent structure with the distorted one in reciprocal space.

The δ strain distorts the structure into an orthorhombic unit cell, with the new lattice parameters a_O and b_O rotated by 45° with respect to the tetragonal a and b axes. Consequently, the Miller indices identifying the peaks differ between the tetragonal and distorted structures, requiring a change of basis for comparison in reciprocal space. The distorted structure generated by ISODISTORT

allows four possible domains, with the following basis sets expressed in terms of the tetragonal basis:

(i) $\{(1,1,0),(-1,1,0),(0,0,-1)\}$
(ii) $\{(1,-1,0),(-1,-1,0),(0,0,1)\}$
(iii) $\{(-1,1,0),(1,1,0),(0,0,-1)\}$
(iv) $\{(-1,-1,0),(1,-1,0),(0,0,1)\}$

The simulation results are presented in Fig. 1(a), where we plot the peak positions in the HK plane at 0 T and 0.6 T. The evolution from 0 T to 0.6 T includes a change in the unit cell volume, referred to as a $e^{\alpha 1/\alpha 2}$ strain. Since the $\alpha 1/\alpha 2$ strain does not modify the symmetry, its presence is always allowed. The Single Crystal software supports changes in lattice parameters, angles, and the volume of the distorted unit cell. By combining these tools, we achieve a good match with the experimental data. The symmetry lowering caused by the δ strain impacts the space group. Based on the group-subgroup relations the e^{δ} strain lowers the symmetry from $I4_1/amd$ to $Fddd$.

[1] P. Santini, S. Carretta, G. Amoretti, R. Caciuffo, N. Magnani, and G. H. Lander, *Multipolar interactions in f-electron systems: The paradigm of actinide dioxides*, Rev. Mod. Phys. **81**, 807 (2009).

[2] D. F. McMorrow, K. A. McEwen, U. Steigenberger, H. M. Rønnow, and F. Yakhou, *X-ray resonant scattering study of the quadrupolar order in* UPd_3, Phys. Rev. Lett. **87**, 057201 (2001).

[3] Y. Kuramoto, H. Kusunose, and A. Kiss, *Multipole orders and fluctuations in strongly correlated electron systems*, J. Phys. Soc. Jpn. **78**, 072001 (2009).

[4] R. Toft-Petersen, T. B. S. Jensen, J. Jensen, M. von Zimmermann, S. Sloth, F. W. Isaksen, N. B. Christensen, Y. Chen, K. Siemensmeyer, H. Kawano-Furukawa, H. Takeya, A. B. Abrahamsen, and N. H. Andersen, *Magnetoelastic phase diagram of* $TbNi_2B_2C$, Phys. Rev. B **97**, 224417 (2018).

[5] R. Sibille, N. Gauthier, E. Lhotel, V. Porée, V. Pomjakushin, R. Ewings, T. Perring, J. Ollivier, A. Wildes, C. Ritter, T. C. Hansen, D. A. Keen, G. Nilsen, L. Keller, S. Petit, and T. Fennell, *A quantum liquid of magnetic octupoles on the pyrochlore lattice*, Nat. Phys. **16**, 546 (2020).

[6] C. Pfleiderer, *Superconducting phases off-electron compounds*, Rev. Mod. Phys. **81**, 1551 (2009).

[7] A. Sakai, K. Kuga, and S. Nakatsuji, *Superconductivity in the ferroquadrupolar state in the quadrupolar Kondo lattice* $PrTi_2Al_{20}$, J. Phys. Soc. Jpn. **81**, 083702 (2012).

[8] E. Rosenberg, M. Ikeda, and I. Fisher, *The nematic susceptibility of the ferroquadrupolar metal* $TmAg_2$ *measured via the elastocaloric effect*, npj Quantum Mater. **9** (2024).

[9] P. Massat, J. Wen, J. Jiang, A. Hristov, Y. Liu, R. Smaha, R. S. Feigelson, Y. Lee, R. M. Fernandes, and I. Fisher, *Field-tuned ferroquadrupolar quantum phase transition in the insulator* $TmVO_4$, Proc. Natl. Acad. Sci. U.S.A. **119**, e2119942119 (2022).

[10] N. Kolmakova, L. Takunov, and O. Shishkina, *Magnetoelastic effects in orthorhombic and tetragonal rare-earth crystals*, Physica (Amsterdam) **352B**, 259 (2004).

[11] P. Morin, J. Rouchy, and D. Schmitt, *Susceptibility formalism for magnetic and quadrupolar interactions in hexagonal and tetragonal rare-earth compounds*, Phys. Rev. B **37**, 5401 (1988).

[12] K. Kishimoto, T. Ishikura, H. Nakamura, Y. Wakabayashi, and T. Kimura, *Antiferroelectric lattice distortion induced by ferroquadrupolar order in* $DyVO_4$, Phys. Rev. B **82**, 012103 (2010).

[13] J. Kjems, W. Hayes, and S. Smith, *Wave-vector dependence of the Jahn-Teller interactions in* $TmVO_4$, Phys. Rev. Lett. **35**, 1089 (1975).

[14] I. Vinograd, K. Shirer, P. Massat, Z. Wang, T. Kissikov, D. Garcia, M. Bachmann, M. Horvatić, I. Fisher, and N. Curro, *Second order Zeeman interaction and ferroquadrupolar order in* $TmVO_4$, npj Quantum Mater. **7**, 1 (2022).

[15] D. Ranaut and K. Mukherjee, *Evolution of field induced magnetic phase attributed to higher order magnetic moments in* $TbVO_4$, Sci. Rep. **13**, 487 (2023).

[16] J. Rivera, *A short review of the magnetoelectric effect and related experimental techniques on single phase (multi-) ferroics*, Eur. Phys. J. B **71**, 299 (2009).

[17] S. Bluck and H. G. Kahle, *Measurement and interpretation of the magnetoelectric effect in* $TbPO_4$, J. Phys. **21**, 5193 (1988).

[18] C. P. Grams, M. Grüninger, and J. Hemberger, *Magnetic field induced critical dynamics in magnetoelectric* $TbPO_4$, Phys. Rev. B **110**, 041106 (2024).

[19] P. Morin, J. Rouchy, and Z. Kazei, *Magnetic and magnetoelastic properties in tetragonal* $TbPO_4$, Phys. Rev. B **50**, 12625 (1994).

[20] C. K. Loong, L. Soderholm, G. L. Goodman, M. M. Abraham, and L. A. Boatner, *Ground-state wave functions of* Tb^{3+} *ions in paramagnetic* $TbPO_4$*: A neutron scattering study*, Phys. Rev. B **48**, 6124 (1993).

[21] J. Coing-Boyat, F. Sayetat, and A. Apostolov, *Caractéristiques cristallographiques, propriétés et structure magnétiques de* $TbPO_4$ *dans la gamme 1, 5 K-300 K*, J. Phys. **36**, 1165 (1975).

[22] A. U. Muller, J. Jakelski, and H. G. Kahle, *Extensive studies on the low-temperature properties of* $TbPO_4$*. III. Birefringence measurements and mean-field calculations*, J. Phys. Condens. Matter **5**, 955 (1993).

[23] M. Rotter, D. M. Le, J. Keller, L. G. Pascut, T. Hoffmann, M. Doerr, R. Schedler, P. F. né Hoffmann, S. Rotter, M. Banks, and N. Klüver, *McPhase users manual (2013)*, https://www2.cpfs.mpg.de/rotter/homepage_mcphase/manual/manual.html.

[24] J. Jensen and A. R. Mackintosh, *Rare Earth Magnetism: Structures and Excitations* (Clarendon Press, Oxford, 1991), http://www.nbi.ku.dk/page40667.htm.

[25] S. Francoual, J. Strempfer, J. Warren, Y. Liu, A. Skaugen, S. Poli, J. Blume, F. Wolff-Fabris, P. C. Canfield, and T. Lograsso, *Single-crystal X-ray diffraction and resonant X-ray magnetic scattering at helium-3 temperatures in high magnetic fields at beamline P09 at PETRA III*, J. Synchrotron Radiat. **22**, 1207 (2015).

[26] W. Nägele, D. Hohlwein, and G. Domann, *Structural and magnetic phase transitions in* $TbPO_4$ *studied by neutron diffraction*, Z. Phys. B Condens. Matter **39**, 305 (1980).

[27] G. Üffinger and A. Kasten, *Specific heat and magnetocaloric effects in* $TbPO_4$ *1. Experiments*, Phys. Status Solidi (b) **128**, 201 (1985).

[28] P. J. Becker, H. G. Kahle, and K. Keller, *The phase diagram of* $TbPO_4$ *measured by linear optical birefringence*, Phys. Status Solidi B **130**, 191 (1985).

[29] A. Maharaj, E. Rosenberg, A. T. Hristov, E. Berg, R. M. Fernandes, I. R. Fisher, and S. A. Kivelson, *Transverse fields to tune an Ising-nematic quantum phase transition*, Proc. Natl. Acad. Sci. U.S.A. **114**, 13430 (2017).

[30] R. M. Fernandes, A. V. Chubukov, and J. Schmalian, *What drives nematic order in iron-based superconductors?*, Nat. Phys. **10**, 97 (2014).

[31] T. Shibauchi, A. Carrington, and Y. Matsuda, *A quantum critical point lying beneath the superconducting dome in iron pnictides*, Annu. Rev. Condens. Matter Phys. **5**, 113 (2014).

[32] A. E. Böhmer, F. Hardy, L. Wang, T. Wolf, P. Schweiss, and C. Meingast, *Superconductivity-induced re-entrance of the orthorhombic distortion in* $Ba_{1-x}K_xFe_2As_2$, Nat. Commun. **6**, 7911 (2015).

[33] R. Grasset, K. Katsumi, P. Massat, H.-H. Wen, X.-H. Chen, Y. Gallais, and R. Shimano, *Terahertz pulse-driven collective mode in the nematic superconducting state of* $Ba_{1--x}K_xFe_2As_2$, npj Quantum Mater. **7**, 4 (2022).

[34] K. R. Islam and A. Chubukov, *Unconventional superconductivity near a nematic instability in a multi-orbital system*, npj Quantum Mater. **9**, 28 (2024).

[35] A. Yamamoto, J. Takeda, T. Koyama, T. Mito, S. Wada, I. Shirotani, and C. Sekine, *Evidence for an antiferroquadrupolar ordering in* YbSb *probed by* ^{121}Sb *and* ^{123}Sb *nuclear magnetic resonances*, Phys. Rev. B **70**, 220402 (2004).

[36] L. Keller, W. Henggeler, and A. Furrer, *Giant quadrupolar interaction in the heavy-fermion compound YbAs*, Europhys. Lett. **26**, 353 (1994).

[37] Y. Iizuka, T. Yamada, K. Hanzawa, and Y. Ōno, *First-principles study of the RKKY interaction and the quadrupole order in the* Pr *1-2-20 systems* PrT_2Al_{20} *(*T = Ti, V*)*, J. Phys. Soc. Jpn. **91**, 074708 (2022).

[38] M. Tsujimoto, Y. Matsumoto, T. Tomita, A. Sakai, and S. Nakatsuji, *Heavy-fermion superconductivity in the quadrupole ordered state of* $PrTi_2Al_{20}$, Phys. Rev. Lett. **113**, 267001 (2014).

[39] E. W. Rosenberg, J.-H. Chu, J. P. C. Ruff, A. T. Hristov, and I. R. Fisher, *Divergence of the quadrupole-strain susceptibility of the electronic nematic system* $YbRu_2Ge_2$, Proc. Natl. Acad. Sci. U.S.A. **116**, 7232 (2019).

[40] P. Morin and Z. Kazei, *Stimulated cooperative jahn-teller effect in* $TmPO_4$, Phys. Rev. B **55**, 8887 (1997).

[41] Z. A. Kazei and R. I. Chanieva, *Magnetoelastic effects in rare-earth vanadates* $YbVO_4$ *and* $HoVO_4$, J. Exp. Theor. Phys. **102**, 266 (2006).

[42] Z. A. Kazei, *Jahn-teller transitions in* $YbXO_4$ *(*X = V*, P) stimulated by a strong magnetic field*, Phys. Solid State **46**, 2249 (2004).

[43] M. Jaime, A. Saul, M. Salamon, V. S. Zapf, N. Harrison, T. Durakiewicz, J. C. Lashley, D. A. Andersson, C. R. Stanek, J. L. Smith, and K. Gofryk, *Piezomagnetism and magnetoelastic memory in uranium dioxide*, Nat. Commun. **8**, 99 (2017).

[44] K. Kimura, T. Katsuyoshi, Y. Sawada, S. Kimura, and T. Kimura, *Imaging switchable magnetoelectric quadrupole domains via nonreciprocal linear dichroism*, Commun. Mater. **1**, 39 (2020).

[45] *Introduction to Complex Mediums for Optics and Electromagnetics*, edited by W. S. Weiglhofer and A. Lakhtakia, SPIE Press Monograph (SPIE Press, Bellingham, WA, 2003), Vol. 123, p. 757.

[46] P. C. Forino, J. Jensen, J. R. Soh, S. Francoual, O. Zaharko, S. Sloth, A. Turrini, R. Feyerherm, K. Prokes, S. Holm-Janas, I. Zivkovic, Y. Liu, A. Magrez, N. B. Christensen, H. M. Rønnow, and R. Toft-Petersen, *Data for article "Inducing ferroquadrupolar order with applied magnetic field in* $TbPO_4$*"*, 10.5281/zenodo.16940462 (2025).

[47] E. du Trémolet de Lacheisserie, *Les coefficients de magnétostriction*, Ann. Phys. (Berlin) **14**, 267 (1970).

[48] W. Böhm, H. G. Kahle, and W. Wüchner, *Spectroscopic study of the crystal field splittings in* $TbPO_4$, Phys. Status Solidi B **126**, 381 (1984).

[49] Y. Hikichi and T. Nomura, *Melting temperatures of monazite and xenotime*, J. Am. Ceram. Soc. **70**, C-252 (1987).

[50] S. Ushakov, K. Helean, A. Navrotsky, and L. Boatner, *Thermochemistry of rare-earth orthophosphates*, J. Mater. Res. **16**, 2623 (2001).

[51] R. S. Feigelson, *Synthesis and single-crystal growth of rare-earth orthophosphates*, J. Am. Ceram. Soc. **47**, 257 (1964).

[52] B. Campbell, H. T. Stokes, D. E. Tanner, and D. M. Hatch, *ISODISPLACE: A web-based tool for exploring structural distortions*, J. Appl. Crystallogr. **39**, 607 (2006).

[53] CrystalMaker Software Ltd., *Single Crystal: A crystal and molecular structures program (2024)*, version 5, Oxford, UK.